machines

MDPI

Article

Defect Suppression Mechanism of CFRP in Longitudinal-Torsional Coupled Ultrasonic Vibration-Assisted Drilling

Guolin Yang [1], Min Zhou [2], Yifan Cao [2], Lehao Zhang [3] and Guofeng Ma [3,*]

[1] Longcheng Laboratory of Intelligent Manufacturing, Changzhou 213164, China
[2] Shanghai Aircraft Manufacturing Co., Ltd., Shanghai 201324, China
[3] College of Vehicle and Traffic Engineering, Henan University of Science and Technology, Luoyang 471003, China
* Correspondence: 9906501@haust.edu.cn

Abstract

Carbon fiber reinforced plastic (CFRP) composites have been widely adopted in the aerospace industry due to their excellent mechanical and physical properties. However, their anisotropy and weak interlaminar bonding make them prone to defects such as delamination and fiber pull-out during conventional drilling (CD). Longitudinal-torsional coupled ultrasonic vibration-assisted drilling (LTC-UAD) integrates axial and circumferential vibrations to suppress hole defects and is considered a promising machining method for improving the quality of holes drilled in CFRP. Based on kinematic analysis, a model for the working rake angle of the main cutting edge is established to obtain the variation law of the maximum working rake angle along the cutting edge. Compared with CD and longitudinal ultrasonic vibration-assisted drilling (L-UAD), LTC-UAD significantly increases and homogenizes the maximum working rake angle of the main cutting edge, which helps optimize its cutting performance. A three-dimensional finite element model of CFRP is constructed to analyze the dynamic fiber removal process under typical fiber orientations. Finally, drilling experiments are performed to observe the hole wall micro-morphology at various fiber angles. The simulation results indicate that ultrasonic vibration causes periodic changes in the fiber cutting angle, subjecting the fibers to a directional shear state and making them more prone to shear fracture. Two-dimensional ultrasonic vibration cutting enhances the directional shear effect, promotes fiber fracture, accelerates chip removal, and improves the quality of the machined surface. Experimental observations confirm LTC-UAD alleviates fiber crushing, bare fibers, and surface cavities with uniform resin coverage. Furthermore, ultrasonic vibration suppresses thrust force. L-UAD and LTC-UAD yield 10.6% and 17.1% reductions via periodic cutting depth variation and facilitated carbon fiber shear fracture.

Keywords: CFRP; longitudinal-torsional coupled ultrasonic vibration; kinematics characteristics; finite element simulation; removal behavior

Check for updates

Academic Editor: Panagiotis Kyratsis

Received: 8 July 2026
Revised: 2 August 2026
Accepted: 4 August 2026
Published: 10 August 2026

Copyright: © 2026 by the authors. Licensee MDPI, Basel, Switzerland. This article is an open access article distributed under the terms and conditions of the Creative Commons Attribution (CC BY) license.

1. Introduction

Carbon fiber reinforced plastic (CFRP) composites are extensively employed for manufacturing structural components of civil airliners and advanced fighter aircraft, owing to their superior strength-to-weight ratio and near-net shape forming performance [1,2]. In aircraft assembly, components of different materials are fastened by bolts and rivets, so numerous assembly holes have to be machined on CFRP composites [3–5]. Featuring a laminated structure, CFRP has low interlaminar bonding strength and obvious anisotropy [6,7].

Conventional drilling (CD) readily causes typical defects such as delamination, tearing, burrs, hole wall pits, and fiber pull-out [8,9]. Accordingly, achieving high-quality hole-making for CFRP components remains a critical technical bottleneck to be addressed urgently in aerospace manufacturing.

Longitudinal ultrasonic vibration-assisted drilling (L-UAD) is a hybrid machining technology that couples one-dimensional longitudinal ultrasonic vibration with CD. Benefiting from the simple and stable structure of its horn, this process has attracted extensive research in recent years [10,11]. Existing studies on L-UAD mainly focus on theoretical modeling and experimental investigation. Drilling force serves as a vital indicator for revealing the material removal mechanism. Li et al. [12] established a mechanical drilling force model for unidirectional CFRP in L-UAD by discretizing drill cutting lips and calculating various component forces. They validated the model via experiments and further analyzed the machined hole surface morphology. To extend the application of drilling force models to thin-walled CFRP structures, Zhang et al. [13] conducted research on L-UAD of thin-walled CFRP. They divided the thrust force model of CD into drill-in and drill-out stages, and established a dynamic thrust force prediction model for L-UAD of thin-walled CFRP by combining dynamic feed rate, critical thrust force theory, and the law of energy conservation. Subsequent drilling experiments on thin-walled CFRPs verified that the average prediction error of the proposed model is 5.43%. Their study also indicated that increasing workpiece stiffness, raising ultrasonic amplitude, and optimizing fixture support can effectively restrain delamination defects. Xu et al. [14] adopted finite element method (FEM) simulation and experiments to study L-UAD for CFRP/Ti stacks. Results show L-UAD reduces cutting forces and hole damage, improves surface quality, and extends tool life compared with CD. These studies have highlighted the vital role of ultrasonic vibration in improving the hole-making quality of CFRP. However, in L-UAD, ultrasonic vibration is applied along the feed direction of the drill bit instead of the cutting direction of the main cutting edge. Although it can moderately improve the cutting conditions of both the main cutting edge and chisel edge, it fails to fully exploit the advantages of ultrasonic vibration in optimizing the cutting performance of the main cutting edge.

It has been widely reported that two-dimensional ultrasonic vibration is superior to L-UAD in machining difficult-to-cut materials [15–17]. Accordingly, researchers developed longitudinal-torsional coupled ultrasonic vibration-assisted drilling (LTC-UAD) to promote drilling performance [18]. For LTC-UAD, ultrasonic vibrations are exerted along both the feed direction and the main cutting direction. The superimposed vibrations improve the cutting performance of chisel edges and enable main cutting edges to perform high-frequency impact and variable-speed cutting, which benefits fiber shearing [19]. At present, most scholars investigate the mechanisms of LTC-UAD of CFRP by experimental methods. To accelerate the practical engineering application of LTC-UAD, Liu et al. [20] experimentally investigated the effects of machining parameters on grinding force and surface roughness in longitudinal-torsional ultrasonic vibration-assisted grinding of CFRP, and performed multi-objective optimization to improve machining performance. Wang et al. [21] investigated LTC-UAD of CFRP/Ti stacked structures. Their findings prove that LTC-UAD effectively reduces thrust force and relieves multi-type hole damage, thereby improving hole integrity and surface quality compared with CD. In addition to drilling parameters, ultrasonic parameters also serve as critical factors affecting hole-making quality. Through kinematic analysis and experimental investigations into the LTC-UAD of CFRP, Ma et al. [22] discovered that a larger torsional-longitudinal amplitude ratio increases the effective working rake angle of the main cutting edge. This effect yields reduced thrust force, suppressed burr formation, and improved surface quality of machined holes, which provides a new perspective for the research on LTC-UAD. Analytical modeling of cutting

force is essential for revealing the underlying machining mechanism of LTC-UAD, as it helps quantitatively clarify the correlation between vibration parameters, tool geometry, and drilling responses. Wang et al. [23] established a dynamic prediction model for the thrust force and torque in LTC-UAD of CFRP/Ti stacks. They verified the model reliability and revealed that vibration and bit geometric parameters primarily determine the dynamic drilling characteristics. A key characteristic of LTC-UAD is the periodic separation between the cutting edge and workpiece material in both the axial and circumferential directions. Accordingly, Li et al. [24] established a kinematic model for the single cutting edge and analyzed the effect of intermittent cutting characteristics on the machining process. The experimental results demonstrate that LTC-UAD reduces the cutting force by 17.8% and the maximum delamination factor by 8.6% compared with CD, which verifies that longitudinal-torsional coupled ultrasonic vibration can effectively suppress drilling defects and remarkably improve the hole-making quality of CFRP.

Nevertheless, theoretical analysis and experimental investigations alone can hardly reveal the microscopic material removal mechanism and damage evolution during cutting. To deeply interpret the dynamic material removal behavior of CFRP, FEM simulation has been adopted to explore the micromechanisms in the drilling process [25]. Xu et al. [26] built a three-dimensional FEM model to explore the material removal mechanisms in elliptical vibration-assisted cutting (EVC). The model was constructed with three parts: a microstructured layer, an equivalent homogeneous material layer, and an infinite element layer. Their results reveal that applying vibration simultaneously along the cutting direction and the direction perpendicular to the cutting direction in EVC can achieve an optimal cutting state, yielding remarkable reductions in cutting force, improved surface integrity, and extended tool life. However, the microstructured layer only contains a single complete fiber layer, which makes it difficult to fully observe the interaction between fibers in adjacent layers. Research concerning FEM simulation of LTC-UAD of CFRP remains limited. Zhang et al. [27] established a three-dimensional thermo-mechanically coupled FEM model incorporating ultrasonic vibration frequency, amplitude, and fiber orientation angle to investigate chip formation in conventional cutting (CC) and one-dimensional ultrasonic vibration-assisted cutting(1D UVC) under fiber orientation angles of 0° and 90°. The results revealed that UVC exhibits distinctly different cutting mechanisms and chip morphologies compared with CC. Unfortunately, other typical fiber orientation angles were not taken into account in their work.

As summarized from the above literature review, most studies evaluate LTC-UAD performance only via indicators such as thrust force and hole wall morphology, while few works reveal the influence mechanism of longitudinal-torsional coupled vibration on the working rake angle and cutting trajectory of the main cutting edge from the tool kinematics perspective. Moreover, research on micro-damage behavior during material removal at typical fiber orientations remains insufficient, and the distinct evolution laws of fiber fracture, interfacial debonding, and matrix crushing under different vibration modes are unclear. Besides, few studies combine FEM simulation with drilling experiments to systematically compare the material removal mechanisms and hole-making performance of CD, L-UAD, and LTC-UAD.

To fill these research gaps, this work first establishes kinematic trajectory equations of the main cutting edge for the three processes to analyze how coupled vibration modulates the tool's actual working rake angle. Second, a CFRP FEM model with fibers, matrix, and interfaces is constructed to compare micro-damage behaviors of the three machining methods at four typical fiber layup angles. Finally, drilling experiments are carried out to characterize hole wall micro-morphology under each condition. Combining kinematic

analysis, FEM simulation, and drilling experiments, this work comprehensively reveals the intrinsic mechanism of LTC-UAD for suppressing drilling defects in CFRP.

2. Kinematics Characteristics Analysis

Figure 1 illustrates the principles of CD, L-UAD, and LTC-UAD. In the CD process, the drill bit performs high-speed rotation and continuous axial feeding motion (Figure 1a). On the basis of CD, L-UAD further applies ultrasonic vibration along the axial direction of the drill bit (Figure 1b). Differently, LTC-UAD simultaneously superimposes axial and circumferential ultrasonic vibrations on the drill bit's rotational and feed movements (Figure 1c). Therefore, for the drill bit in the LTC-UAD, its cutting edge performs periodic composite motion in both the axial and circumferential directions simultaneously.

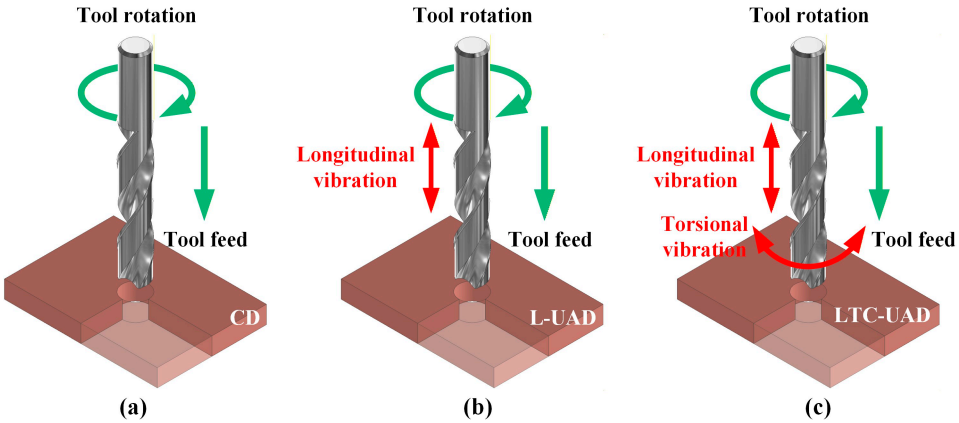

Figure 1. Schematic diagrams of (**a**) conventional drilling (CD), (**b**) longitudinal ultrasonic vibration-assisted drilling (L-UAD), and (**c**) longitudinal-torsional coupled ultrasonic vibration-assisted drilling (LTC-UAD).

In the process of LTC-UAD, the actual rotation angle of the drill bit is the superposition of the spindle-driven rotation angle and the additional rotation angle induced by torsional ultrasonic vibration. Since the spindle rotates at a constant speed, the actual rotation angle φ of the drill bit within time t can be defined as follows:

$$\varphi = \omega_0 \, t + \varphi_a \sin(2\pi f t + \varphi') \tag{1}$$

$$\omega_0 = 2\pi n / 60 \tag{2}$$

where n represents the spindle speed, φ_a represents the angular amplitude of torsional vibration, f represents the ultrasonic vibration frequency, φ' represents the phase difference between the torsional and longitudinal vibrations, and ω_0 represents the rotating angular velocity of the spindle.

Accordingly, the kinematic trajectory equations for the main cutting edge of the drill bit under the LTC-UAD are derived as follows:

$$\begin{aligned} x &= R\cos(\varphi), \\ y &= R\sin(\varphi), \\ z &= Ft + A\sin(2\pi f t), \end{aligned} \tag{3}$$

where R represents the radius of an arbitrary point on the main cutting edge of the drill bit, F represents the axial feed speed of the drill bit, and A represents the longitudinal amplitude of ultrasonic vibration.

Based on the corresponding trajectory equations, the trajectories of the selected point on the main cutting edge of the drill bit under CD, L-UAD, and LTC-UAD were plotted

using MATLAB (R2020b), as illustrated in Figure 2. The motion trajectories of the main cutting edge differ remarkably under the three machining conditions. In the process of CD, the motion trajectory of the main cutting edge presents a helix along the feed direction, as shown in Figure 2a. For L-UAD, the introduction of longitudinal ultrasonic vibration superimposes a sinusoidal curve onto the helix to form the final trajectory of the main cutting edge, as illustrated in Figure 2b. In LTC-UAD, longitudinal vibration is applied along the drill axial direction while torsional vibration acts in the circumferential direction. Accordingly, under a specific set of processing parameters, the motion trajectory of the main cutting edge is the geometric superposition of an elliptical curve and a helix, as demonstrated in Figure 2c.

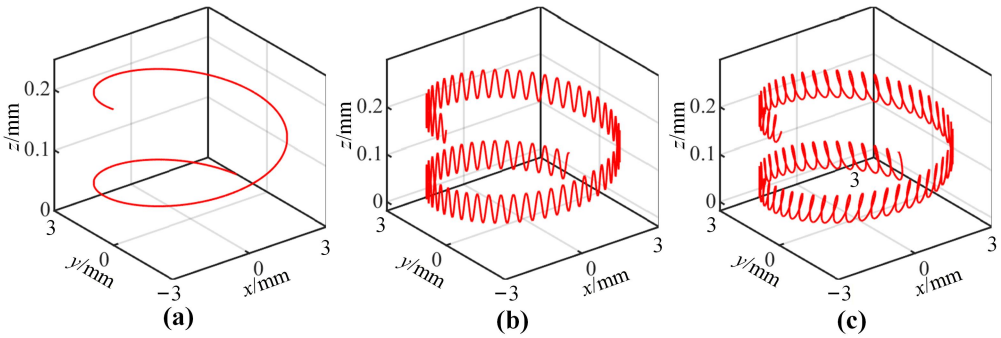

Figure 2. Schematic diagrams of cutting trajectories: (**a**) CD; (**b**) L-UAD; (**c**) LTC-UAD (n = 10,000 r/min, f = 8000 Hz, $\varphi_a = \pi/60$, $\varphi' = \pi/4$, R = 2 mm, F = 25 mm/s, A = 0.03 mm).

In LTC-UAD, the introduction of longitudinal and torsional ultrasonic vibrations leads to periodic variations of the cutting angle of the main cutting edge in both spatial and temporal domains. Based on classical cutting theory, the working rake angle of the main cutting edge of the drill bit γ_e can be written as:

$$\gamma_e = \gamma_{ox} + \delta \tag{4}$$

$$\tan \gamma_{ox} = \tan \beta_x / \sin k_{rx} + \tan \lambda_{rx} \cos k_{rx} \tag{5}$$

$$\delta = \arctan (v_z / v_\tau) \cos k_{rx} \tag{6}$$

where γ_{ox} represents the static rake angle of an arbitrary point on the main cutting edge, k_{rx}, λ_{tx}, and β_x represent the cutting edge angle, edge inclination angle, and helical angle for an arbitrary point on the main cutting edge.

Substitute the parameters: n = 2000 r/min, F = 20 mm/min, f = 27.5 kHz, d = 6 mm, r_0 = 0.45 mm, β = 30° and p = 59° into Equations (4)–(6). The variation curves of the working rake angle at an arbitrary point on the main cutting edge under CD, L-UAD and LTC-UAD are plotted in Figure 3.

As shown in Figure 3a, the working rake angle of CD remains constant throughout the cutting process and shows no variation with cutting time t. Along the main cutting edge from the drill outer edge to the intersection with the chisel edge, the working rake angle decreases gradually and becomes negative near the chisel edge, which is an intrinsic limitation of CD. For L-UAD and LTC-UAD, as shown in Figure 3b,c, the working rake angle changes periodically with cutting time t, and its distribution against radius r differs at different moments. Comparative results reveal that the working rake angle fluctuates at a higher frequency in LTC-UAD.

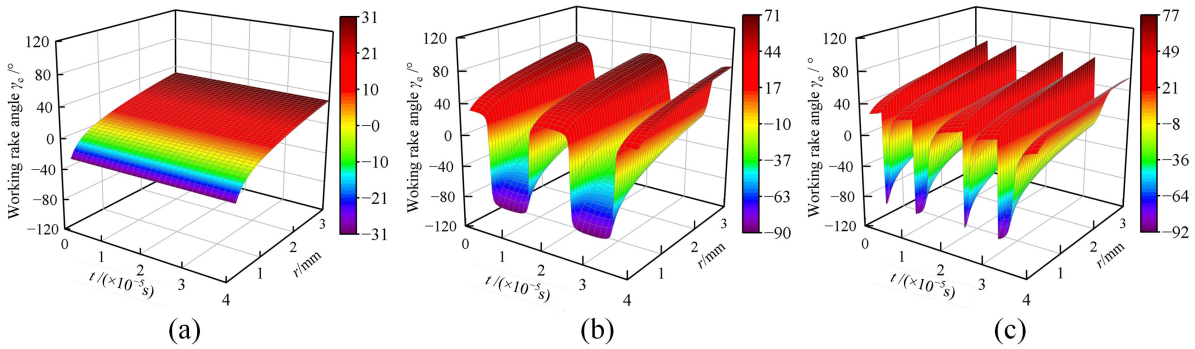

Figure 3. Working rake angle of the main cutting edge: (**a**) CD; (**b**) L-UAD; (**c**) LTC-UAD.

In separated cutting, only the working rake angle within the actual cutting interval needs to be considered. The influence law of ultrasonic vibration on the working rake angle can be investigated according to the variation of the maximum working rake angle of the main cutting edge. Therefore, based on the data in Figure 3, the variation curve of the maximum working rake angle of the main cutting edge with the corresponding radius r is plotted, as shown in Figure 4. Compared with CD, the maximum working rake angle of the main cutting edge is significantly increased under the two types of UAD, and the maximum working rake angle reaches the highest value in LTC-UAD. In addition, the increment of the maximum working rake angle is more prominent near the chisel edge. This reduces the variation range of the working rake angle along the main cutting edge and achieves a more uniform distribution, which is beneficial to improving the cutting performance of the main cutting edge.

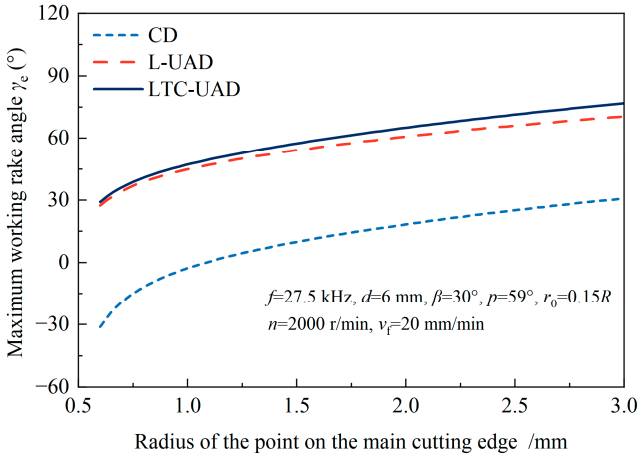

Figure 4. Variation of the maximum working rake angle of the main cutting edge.

3. FE Modeling of Ultrasonic Vibration Cutting for CFRP

3.1. Modeling of CFRP and Cutting Tool

To characterize the micro-morphology and macroscopic mechanical properties of materials, a representative volume element (RVE) of CFRP was constructed. The RVE consists of matrix, carbon fibers, and fiber-matrix interfaces with an edge length of 8 μm. The cylindrical carbon fibers have a diameter of 7 μm, yielding a fiber volume fraction of approximately 60%. Zero-thickness cohesive elements were adopted to model the interfacial phase. To guarantee simulation precision while restricting the total number of elements, a local geometric model of the workpiece covering two unidirectional plies within the cutting zone was established according to the micrometer-scale dimensions of carbon fibers and resin matrix. The thickness of each unidirectional ply equals the edge

length of the RVE. The three-dimensional geometric dimensions of the CFRP workpiece model are 250 μm (length) × 200 μm (height) × 16 μm (thickness).

The cutting tool possesses a rake angle of 20°, a clearance angle of 11°, a cutting edge radius of 10 μm, and a cutting edge length of 30 μm. Since the elastic modulus of the tool material is several times larger than that of the workpiece, the tool deformation during cutting can be neglected. Accordingly, the tool was defined as a 3D discrete rigid body in the finite element model. Figure 5 presents the established 3D orthogonal cutting model under a fiber cutting angle of 90°, and Table 1 summarizes the geometric parameters of the workpiece and cutting tool.

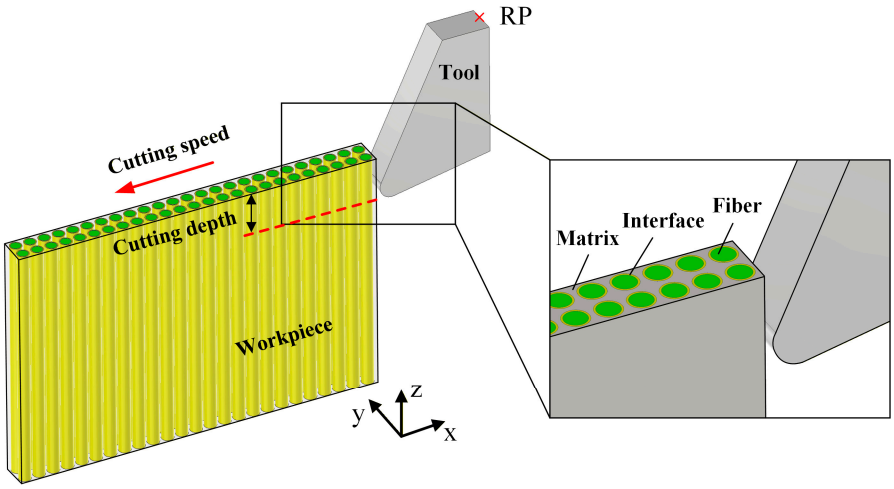

Figure 5. Schematic of the 3D finite element model for orthogonal cutting of CFRP at a fiber cutting angle of 90°.

Table 1. Parameters of the workpiece and cutting tool in the simulation model.

	Parameters	Value
Workpiece	Side length of representative volume element (RVE) (μm)	8
	Fiber diameter (μm)	7
	Fiber volume fraction	60%
	Overall dimension (μm)	250 × 200 × 16
Cutting tool	Rake angle, clearance angle (°)	20, 11
	Edge radius (μm)	10
	Cutting edge length (μm)	30

3.2. Definition of Material Property

The constitutive behavior of carbon fiber is defined via the VUMAT in ABAQUS, which is invoked throughout the numerical calculation. A local coordinate system is established within the fiber domain, and the anisotropic material orientation is assigned along the fiber axial direction. The matrix adopts thermosetting epoxy resin with a density of 1200 kg/m^3; its elastic response is defined as isotropic, and the Johnson-Cook constitutive model is adopted to characterize its plastic behavior. The properties of carbon fiber and resin matrix are listed in Table 2 and Table 3, respectively. The relevant parameters of fiber and resin matrix adopted in the model are provided by the COMAC Composite Materials Center and determined based on References [25,28].

Table 2. Mechanical properties of carbon fiber [28].

Parameters	Value
Elastic modulus (GPa)	E_{11} = 231, E_{22} = 15
Shear modulus (GPa)	G_{12} = G_{13} = 15, G_{23} = 7
Poisson's ratio	v_{12} = 0.2
Tensile strength (MPa)	X_t = 4620, Y_t = 1500
Compressive strength (MPa)	X_c = 3960, Y_c = 3340
Shear strength (MPa)	S = 380

Table 3. Properties of resin matrix [25].

Parameters	Value
Elastic modulus (GPa)	E_{m} = 3.2
Yield strength (MPa)	σ_{y0}^{m} = 225
Poisson's ratio	v_{m} = 0.33
J-C parameters	A = 225, B = 72, m = 0.304, n = 0.2, c = 0.1

3.3. Definition of Boundary Conditions and Interaction Properties

Full fixed constraints are applied to the bottom surface, left surface, and lower half of the right surface of the workpiece. To avoid rotation of the cutting tool during the cutting process, the rotational degrees of freedom of the tool reference point (RP) in the x, y, and z directions are fully constrained. Three types of contact pairs exist during the cutting of CFRP composites: contact between tool and carbon fiber, contact between tool and epoxy matrix, and contact between fiber and matrix. All three contact pairs are defined as general contact. The penalty method is adopted to describe tangential contact behavior, while hard contact is assigned for normal contact to prevent element interpenetration. The fiber-matrix interface is further characterized by cohesive contact to simulate bond-slip responses. The damage initiation is specified, and energy-based linear softening is adopted for damage evolution. The Benzeggagh-Kenane mixed-mode criterion is utilized to capture mixed-mode interfacial fracture. Detailed parameters for fiber-matrix contact are listed in Table 4.

Table 4. Contact properties between fiber and resin [29].

Parameters	Value
Stiffness coefficients	$K_{\mathrm{nn}} = K_{\mathrm{ss}} = K_{\mathrm{tt}} = 1 \times 10^5$
Initial damage strength	Normal only = 50 Shear-1 Only = Shear-2 Only = 75
Benzeggagh-Kenane exponent	1.45
Fracture energy	Normal Fracture Energy = 0.002 1st Shear Fracture Energy = 0.006 2st Shear Fracture Energy = 0.006

In this study, a two-dimensional orthogonal cutting model is adopted to reproduce the cutting behavior of the drill's main cutting edge, and this simplification is justified by two key reasons. First, microscale fiber-matrix fracture and interfacial debonding only occur within the localized cutting zone of the main cutting edge. The orthogonal cutting model can effectively capture the instantaneous material removal mechanism at the micrometer scale while drastically reducing the computational cost induced by massive mesh elements. Second, the core objective of the finite element simulation is to compare fiber fracture modes

and subsurface damage evolution under CC, 1D UVC, and two-dimensional ultrasonic vibration cutting (2D UVC), rather than reconstructing the full dynamic drilling process.

Nevertheless, these simplifications inevitably lead to discrepancies between simulated predictions and practical drilling. The orthogonal cutting model omits two critical factors in real drilling operations: the extrusion and cutting effect of the chisel edge on hole-bottom materials, and the continuous helical feed motion of the entire drill bit. Accordingly, the model fails to characterize cumulative damage induced by repeated cutting of the chisel edge, as well as continuous chip evacuation throughout the full penetration of the drill bit. Furthermore, only a single instantaneous cutting pass is simulated in this work, so the superposition effect of multiple cutting cycles on micro-defects of the hole wall cannot be reflected. In addition, the simplified boundary constraints can hardly reproduce the actual restraint state of materials at the hole bottom. In summary, the simulation results are only intended to qualitatively reveal the inherent differences in fiber-matrix removal mechanisms among the three machining methods, and quantitative indicators including surface quality and fiber deformation magnitude cannot be directly correlated with macroscopic data obtained from complete drilling experiments.

3.4. Definition of Cutting Parameters

To replicate the cutting behavior of the main cutting edge in drilling as accurately as possible via orthogonal cutting simulation, the cutting speed and cutting depth in the orthogonal cutting model are assigned equal to the tangential cutting velocity and feed per tooth derived from the drilling condition: drill diameter d = 6 mm, spindle speed n = 2000 r/min, feed speed F = 80 mm/min. According to the above drilling parameters, the theoretical feed per revolution can be calculated. The axial feed distance of the drill bit per revolution is 40 μm. Since the drill bit possesses two main cutting edges, the axial cutting depth for a single main cutting edge is 20 μm. For both 1D UVC and 2D UVC simulations, the ultrasonic frequency is fixed at 27.5 kHz, with an x-direction vibration amplitude of 4.8 μm and y-direction amplitude of 12 μm. All cutting and ultrasonic vibration parameters adopted in the simulation model are summarized in Table 5.

Table 5. Cutting and ultrasonic vibration parameters used in the simulation.

Machining Condition	Cutting Speed v_c (m/min)	Cutting Depth a_p (μm)	Ultrasonic Frequency f (kHz)	X-Direction Amplitude (μm)	Y-Direction Amplitude (μm)
CC	37.68	20	-	-	-
1D UVC	37.68	20	27.5	-	12
2D UVC	37.68	20	27.5	4.8	12

4. Experimental Conditions and Methods

4.1. Experimental Setup and Conditions

All drilling experiments were carried out on a three-axis CNC machining center (Ninghua NHM800, Ninghua Machine Tool Co., Ltd., Beijing, China) with a spindle speed up to 10,000 r/min. As shown in Figure 6, the ultrasonic vibration setup consists of an ultrasonic generator, power transmission unit, and self-developed ultrasonic tool holders. As the core component of the vibration system, the tool holder is composed of a base body, piezoelectric transducer, and horn. The transducer transforms electrical energy into high-frequency mechanical vibration, and the horn adjusts and amplifies the vibration amplitude to actuate the drill bit. The laser displacement sensor (Keyence LK-H025, KEYENCE Corporation, Osaka, Japan) was employed to measure the drill bit's longitudinal and torsional amplitudes under no-load conditions.

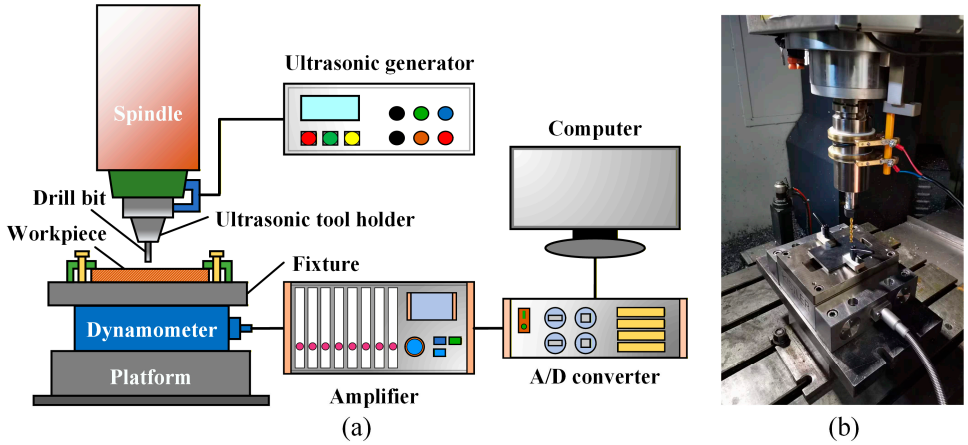

Figure 6. (**a**) Schematic diagram and (**b**) experimental setup of UAD.

The workpiece employed in the experiments is a 5 mm-thick CFRP laminate composed of 28 prepreg plies stacked in the sequence of $[-45/0_2/45/0/90/0]_{S2}$, as illustrated in Figure 7. Prior to the experiment, the CFRP laminate was cut into specimens with dimensions of 100 mm × 75 mm to facilitate clamping and subsequent inspection of hole quality. A TiN-coated cemented carbide twist drill bit with a nominal diameter of 6 mm, a point angle of 118° and a helix angle of 33° was utilized in the drilling experiments.

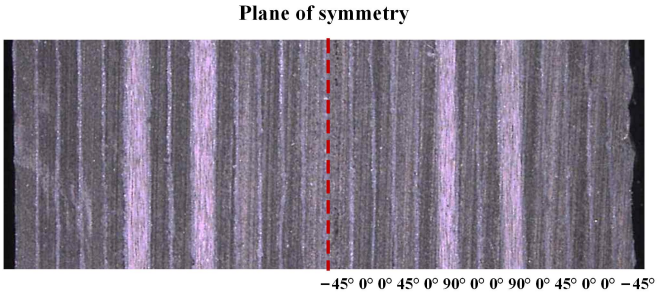

Figure 7. Cross-sectional structure of CFRP laminates.

4.2. Experimental Design

With identical drilling parameters maintained, three types of drilling experiments were carried out separately, namely CD, L-UAD, and LTC-UAD. The longitudinal vibration amplitude was kept consistent for both L-UAD and LTC-UAD, and all machining parameters are listed in Table 6. The machining parameters used in this study are summarized based on experimental experience, which can give full play to the effect of ultrasonic vibration to a large extent. Each group of experiments was repeated three times to reduce experimental errors. To eliminate the influence of tool wear on results, a new drill bit was replaced after machining each hole.

Table 6. Machining parameters for drilling experiments with various ultrasonic vibration forms.

Parameters	Value
Spindle speed n (r/min)	2000
Feed rate F (mm/min)	80
Ultrasonic frequency f (kHz)	CD: 27.8 L-UAD: 27.6 LTC-UAD: 27.5
Longitudinal amplitude A_L (μm)	12
Torsional amplitude A_T (μm)	4.8

5. Results and Discussions

5.1. Simulation Analysis of Removal Behavior of CFRP Under Different Vibration Forms

5.1.1. 0° Fiber Orientation

As shown in Figure 8, for the case of a 0° fiber orientation under CC condition, the upward component force generated by the positive rake angle of the tool peels the material of the cutting layer from the substrate and induces bending deformation. The material is finally removed via bending fracture. In addition, the fiber layers in contact with the cutting edge radius bear downward compressive force and are eventually crushed onto the machined surface by the edge radius and the flank face.

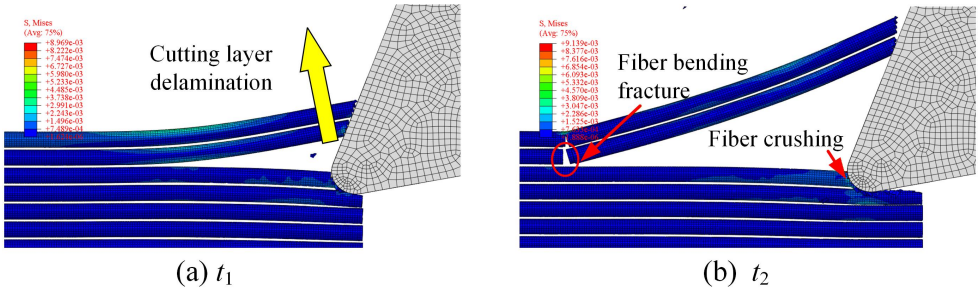

Figure 8. Simulation results of CC for 0° fiber orientation.

As shown in Figure 9, the deformation mode of fibers and resin under 1D UVC remains interlayer separation. It should be noted that, as illustrated in Figure 9a, when the cutting edge contacts the fibers, the fibers first undergo axial crushing because the cutting velocity direction is parallel to the fiber axial direction at this moment. As presented in Figure 9b,c, the motion of the cutting edge moving away from the workpiece along a sinusoidal trajectory accelerates the delamination of the cutting layer from the substrate, and fiber bending fracture occurs during this process. When the tool approaches the workpiece again in the next vibration cycle, the edge radius and flank face extrude the machined surface. It can be observed from Figure 9d that three layers of fibers are fractured on the machined surface, which may degrade the quality of the machined surface.

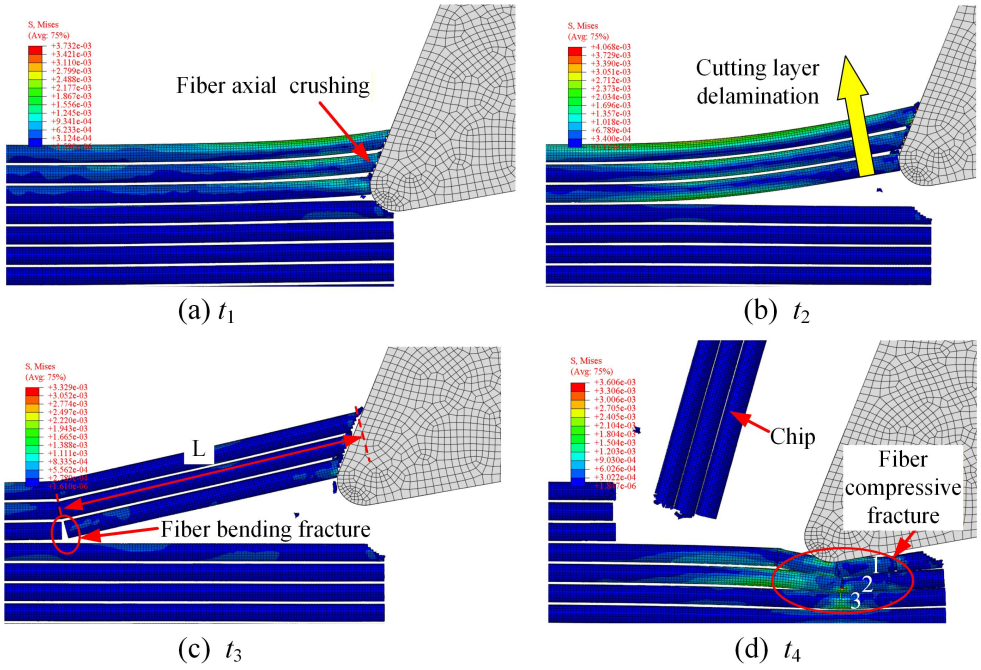

Figure 9. Simulation results of 1D UVC for 0° fiber orientation.

As displayed in Figure 10a,b, the fiber removal behavior under 2D UVC is similar to that in 1D UVC. The cutting layer material first experiences axial crushing and delamination before bending fracture takes place. As shown in Figure 10c, the bending fracture of the cutting layer material occurs in the second vibration cycle, and the fractured fibers possess a longer length. As demonstrated in Figure 10d, two layers of fibers fracture on the machined surface under the extrusion of the edge radius and flank face in the subsequent vibration cycle.

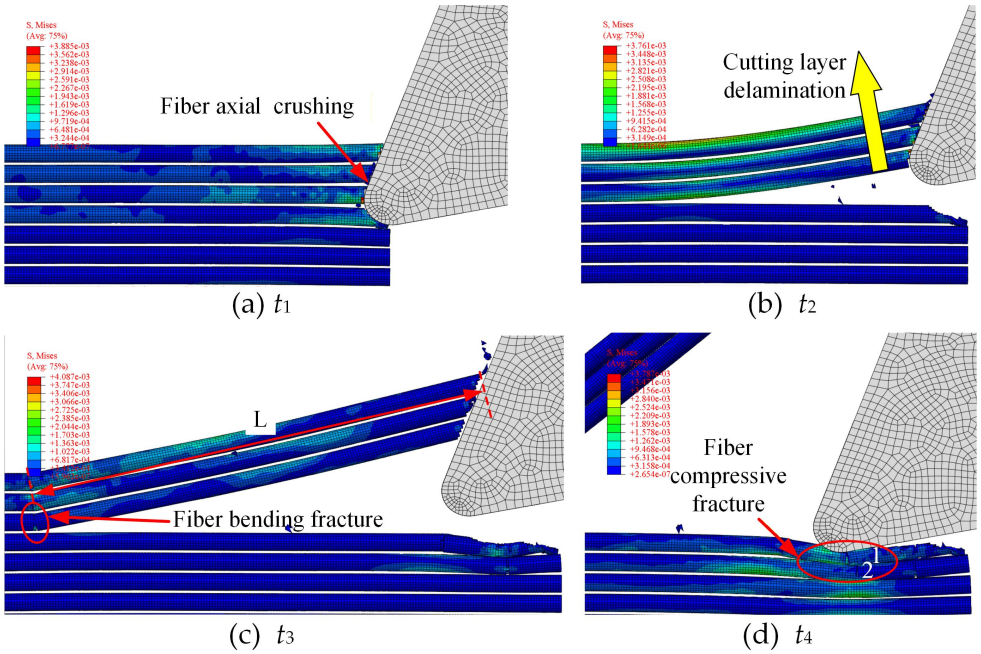

Figure 10. Simulation results of 2D UVC for 0° fiber orientation.

5.1.2. 45° Fiber Orientation

As shown in Figure 11a, under CC conditions with a 45° fiber orientation, the fibers ahead of the cutting edge first experience shear fracture at point A under the compression of the edge radius. As the tool proceeds forward, the severed fibers accumulate near the edge radius on the rake face and extrude the uncut fibers behind them. At this stage, the maximum stress of the uncut fibers is located above the machined surface. Accordingly, fiber fracture occurs at point B above the machined surface, as illustrated in Figure 11b, which results in inconsistent lengths of residual fibers on the machined surface and degraded machined surface quality. As presented in Figure 11c, the unremoved fiber segment BC undergoes bending fracture at point C due to the extrusion of the edge radius. The fractured BC fiber segment cannot be evacuated promptly and adheres to the machined surface under the squeezing action of the flank face, as demonstrated in Figure 11d.

As shown in Figure 12a, under 1D UVC, the cutting depth varies periodically since ultrasonic vibration is applied along the cutting depth direction. The cutting velocity direction under ultrasonic vibration is nearly perpendicular to the fiber axial direction, and the fibers undergo shear fracture perpendicular to their axis, yielding smooth fracture sections. The included angle α between the plane of adjacent fiber fracture sections and the horizontal plane is relatively large, so the fracture surfaces extend deep beneath the machined surface. As illustrated in Figure 12b, the tool exerts a lifting effect on the chips when moving away from the workpiece, which facilitates chip evacuation. This advantage is more prominent for drilling processes with semi-closed cutting zones. As presented in Figure 12c, the fibers ahead of the cutting edge are sheared off under the combined cutting action and high-frequency impact of the cutting edge. As the tool feeds forward

continuously, the severed fibers slide along the fiber orientation under the extrusion of the rake face and edge radius, and finally form chips. The above fiber removal behavior eventually produces a serrated machined surface, as demonstrated in Figure 12d.

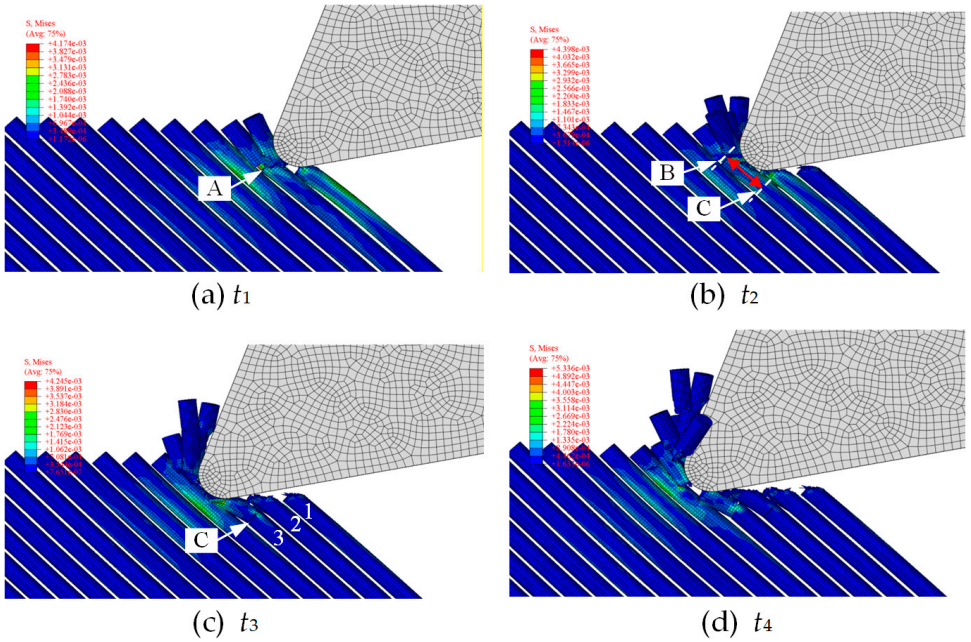

Figure 11. Simulation results of CC for 45° fiber orientation.

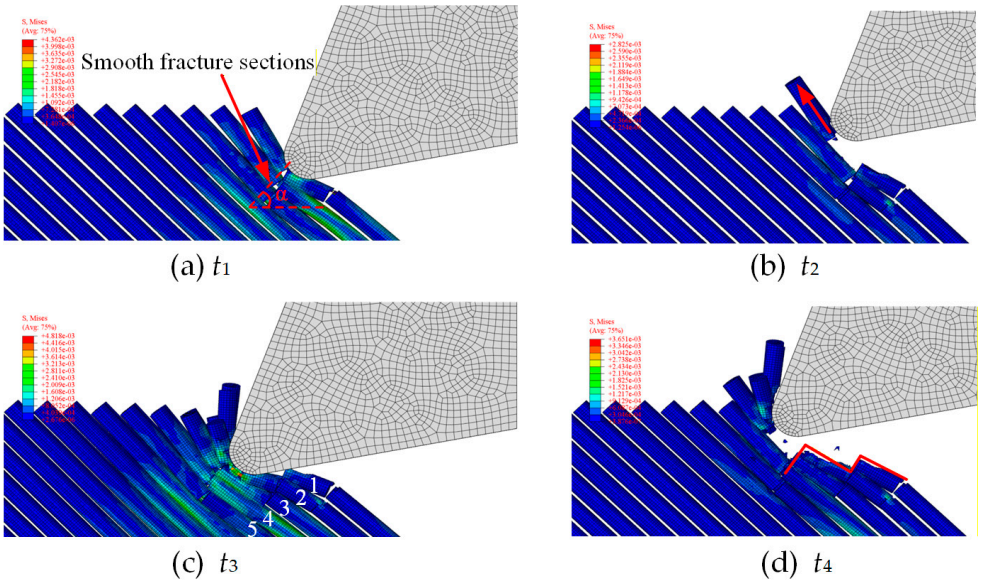

Figure 12. Simulation results of 1D UVC for 45° fiber orientation.

As shown in Figure 13a, the unique elliptical motion trajectory of the cutting edge in 2D UVC makes the cutting velocity direction nearly perpendicular to the fiber axial direction. Accordingly, fibers are more prone to shear fracture with smooth fracture sections. In addition, the elliptical tool trajectory reverses the friction direction between the rake face and chips, which facilitates chip evacuation from the cutting zone, as illustrated in Figure 13b,d. Compared with Figure 12c, the number of fractured fibers in Figure 13c remains identical, while fiber deformation in and around the cutting zone is significantly less severe. Under 2D UVC, reliable fiber fracture can be realized. Meanwhile, the smaller included angle α results in a shallower extension depth of fiber fracture planes beneath the

machined surface. Consequently, the serration size on the machined surface is reduced, which contributes to superior surface quality, as demonstrated in Figure 13d.

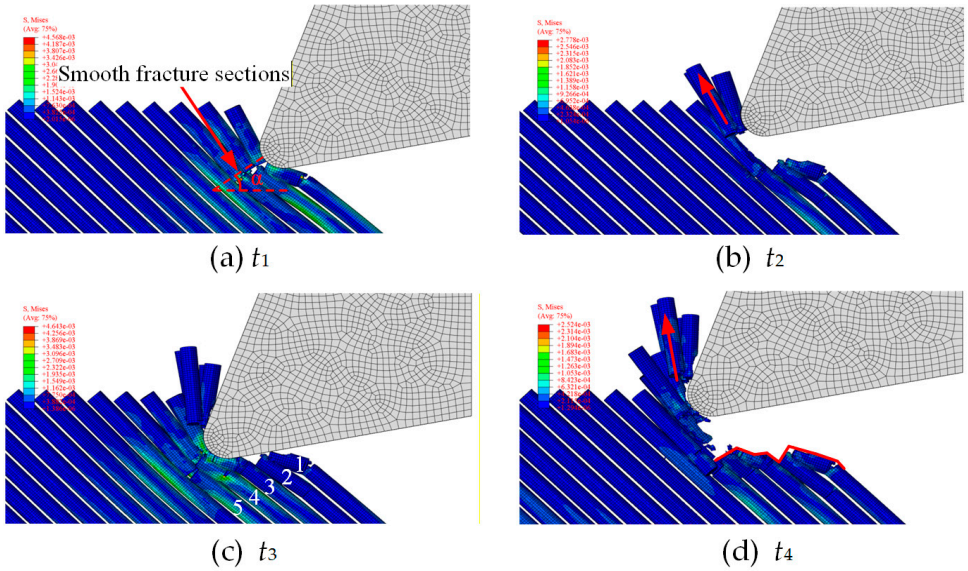

Figure 13. Simulation results of 2D UVC for 45° fiber orientation.

5.1.3. 90° Fiber Orientation

For a 90° fiber orientation under CC conditions, the cutting velocity is horizontal and perpendicular to the fiber axial direction, and the cutting depth remains constant throughout the cutting process. As the tool advances, fibers deflect and bend under the horizontal extrusion of the edge radius; fiber fracture initiates once the bending stress reaches the ultimate tensile strength. As shown in Figure 14a, material removal is realized via fiber bending fracture, which requires considerable fiber deformation to reach the strength limit (the fiber deformation along the x-direction is 10.52 μm). As illustrated in Figure 14b, the maximum bending stress of the fibers occurs at a relatively deep position below the cutting edge. In addition, fibers bear heterogeneous loading states, leading to randomly distributed fracture positions beneath the machined surface (the fiber fracture depth d_p = 16.19 μm). This phenomenon ultimately deteriorates the quality of the machined surface.

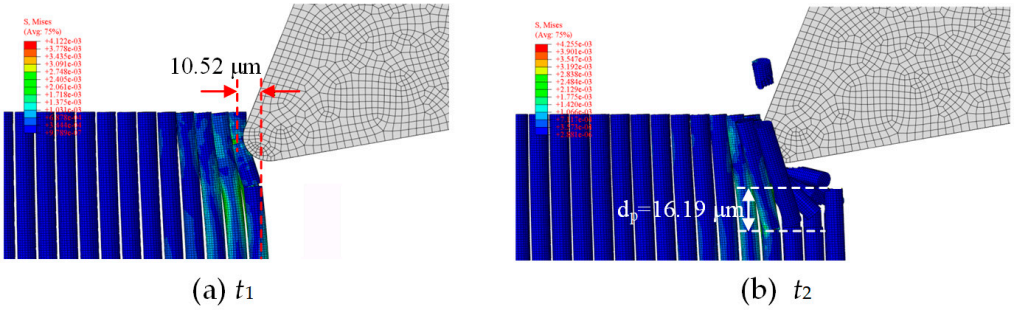

Figure 14. Simulation results of CC for 90° fiber orientation.

As shown in Figure 15a, fibers are no longer removed by bending fracture during 1D UVC. Instead, crushing, shear fracture, and bending fracture of fibers occur under the combined cutting action and high-frequency impact of the cutting edge, which drastically reduces the fiber deformation at fracture (the fiber deformation along the x-direction is 5.83 μm). As illustrated in Figure 15b, compared with CC, the actual fiber fracture position becomes shallower under 1D UVC (the fiber fracture depth d_p = 9.05 μm), which contributes to the improvement of machined surface quality. As presented in Figure 15c, when the tool

moves away from the workpiece surface, the fractured fibers adjacent to the rake face are evacuated from the cutting zone under the action of the rake face, while the broken fibers in region A beneath the cutting edge remain on the machined surface. In the next ultrasonic vibration cycle, as the tool moves toward the workpiece again, the fiber segments left on the machined surface are pressed onto the finished surface by the flank face, as demonstrated in Figure 15d.

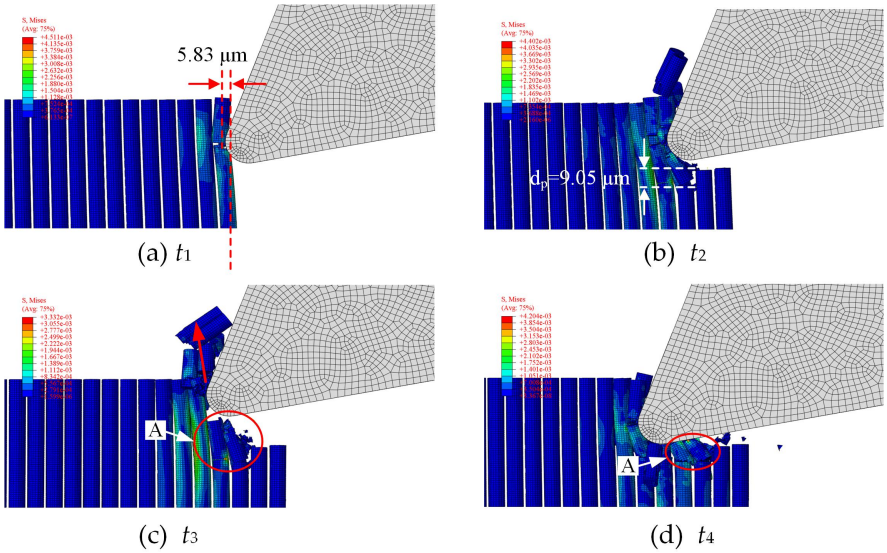

Figure 15. Simulation results of 1D UVC for 90° fiber orientation.

As shown in Figure 16a, the fiber removal behavior under 2D UVC is similar to that in 1D UVC, and the x-direction fiber deformation at the initial fracture is reduced to 4.65 μm. As illustrated in Figure 16b, the depth of fracture positions during fiber bending fracture is further decreased (fiber fracture depth d_p = 7.96 μm). As presented in Figure 16c,d, driven by the cutting edge and rake face under the elliptical tool trajectory, fractured fibers detach more easily from the machined surface. This prevents them from being extruded onto the machined surface by the flank face in the subsequent vibration cycle.

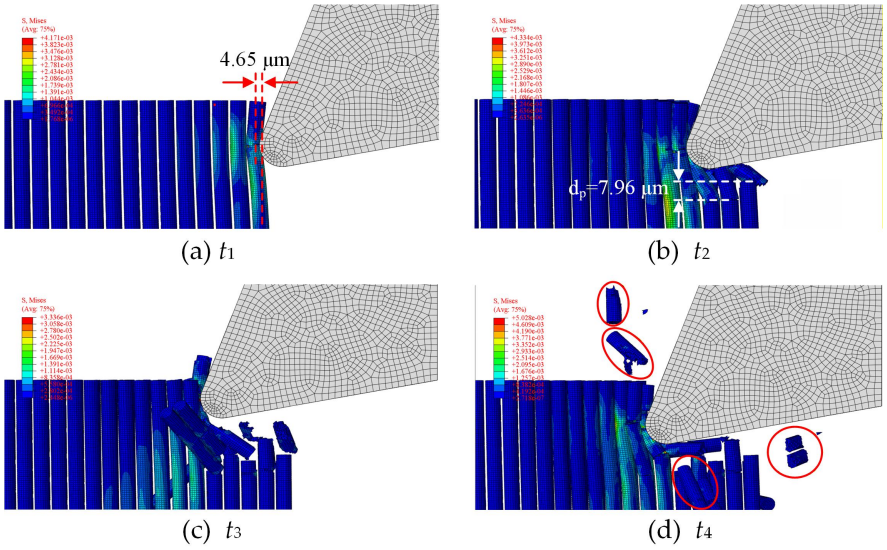

Figure 16. Simulation results of 2D UVC for 90° fiber orientation.

5.1.4. 135° Fiber Orientation

For a 135° fiber orientation under CC conditions, four fibers fracture under the pushing extrusion of the rake face as the tool advances. The included angle between the plane of fiber fracture sections and the horizontal plane is 26.62°, as shown in Figure 17a. As the tool proceeds forward continuously, fibers are severed sequentially, and the fractured fibers accumulate around the cutting edge, as illustrated in Figure 17b.

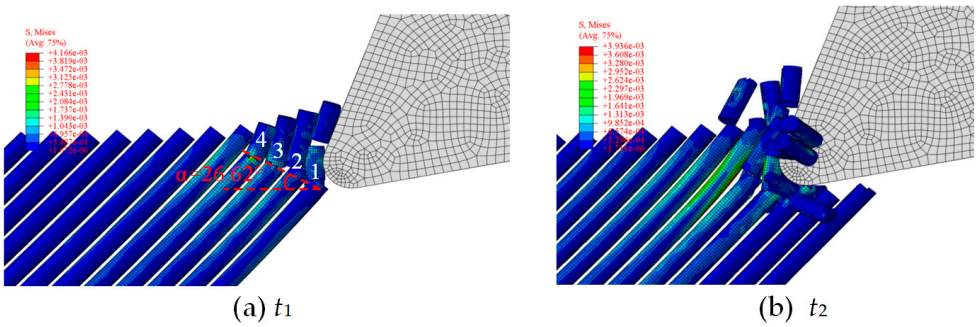

Figure 17. Simulation results of CC for 135° fiber orientation.

Under 1D UVC, the introduction of ultrasonic vibration facilitates fiber fracture, and five fibers ahead of the cutting edge break within the first vibration cycle. The sinusoidal cutting trajectory increases the included angle between the plane of fiber fracture sections and the horizontal plane to 41.9°, as shown in Figure 18a. In the subsequent ultrasonic vibration cycle, when the tool moves toward the workpiece, the fractured fibers in region A are extruded onto the machined surface by the flank face, as illustrated in Figure 18b.

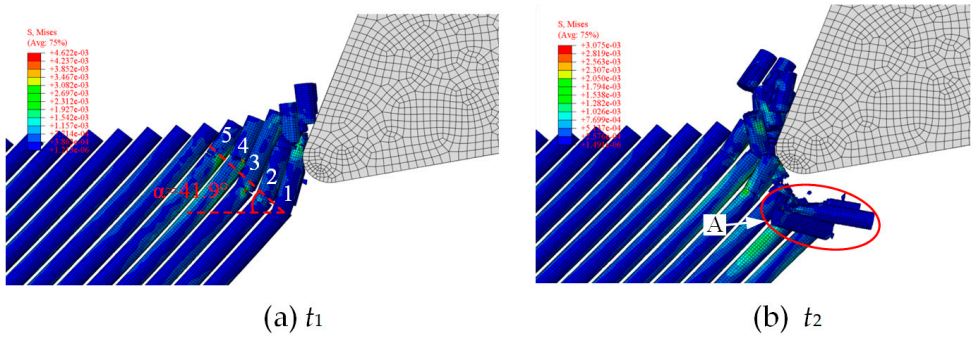

Figure 18. Simulation results of 1D UVC for 135° fiber orientation.

As presented in Figure 19a, when 2D ultrasonic vibrations are applied, six fibers ahead of the cutting edge fracture under the combined cutting action and high-frequency impact of the cutting edge, and the included angle between the plane of fiber fracture sections and the horizontal plane reaches 36.79°. As demonstrated in Figure 19b, the elliptical motion trajectory drives all fractured fibers to evacuate from the machined surface under the pushing extrusion of the cutting edge and rake face. This avoids the secondary extrusion by the edge radius and flank face in the next vibration cycle, which contributes to the improvement of machined surface quality.

5.2. Micro-Morphology of Hole Wall

The CFRP adopted in the experiments is stacked by 28 unidirectional fiber layers with different fiber orientations, so the fiber orientation varies at different positions on the hole wall. To make a comparison with the simulation results, four typical regions with fiber orientations of 0°, 45°, 90° and 135° on the hole wall were selected as the observation areas.

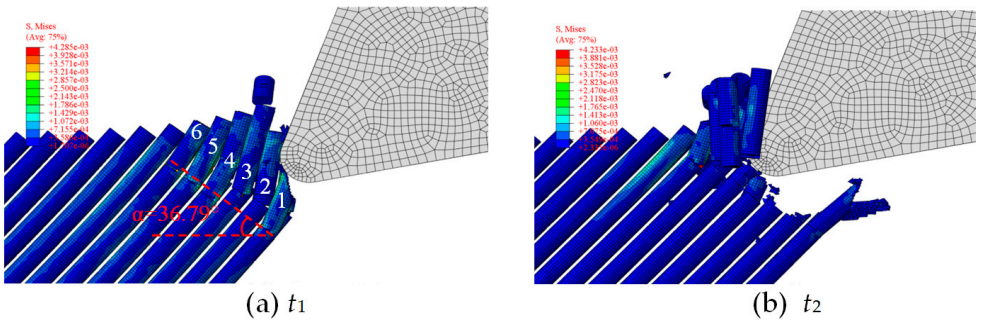

Figure 19. Simulation results of 2D UVC for 135° fiber orientation.

5.2.1. Micro-Morphology of Hole Wall with 0° Fiber Orientation

Figure 20 displays the hole wall micro-morphology under CD, L-UAD, and LTC-UAD at a fiber orientation of 0°. Obvious fiber cracks, crush, and fragments can be observed in Figure 20a. In Figure 20b,c, residual fiber fragments on the hole wall are greatly reduced, accompanied by much flatter fiber fracture cross-sections. This observation differs from the simulation results presented in Section 5.1.1. The reason lies in the fact that the elliptical cutting trajectory of the minor cutting edge strengthens its scraping and polishing effects on the hole wall. This facilitates the removal of residual fiber fragments and chips from the hole wall, while uniformly smearing resin over the machined surface.

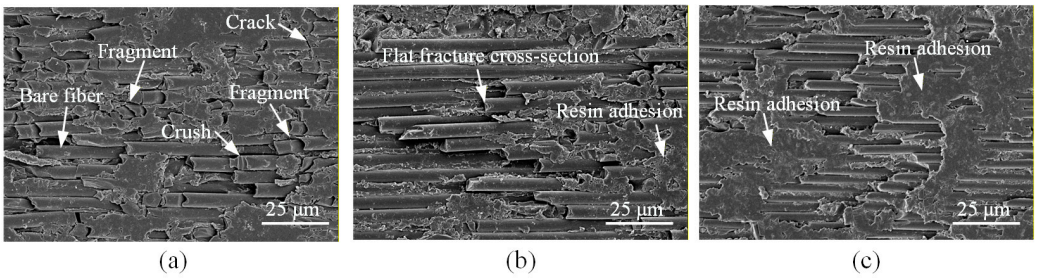

Figure 20. Micro-morphology of hole wall with 0° fiber orientation: (**a**) CD, (**b**) L-UAD, (**c**) LTC-UAD.

5.2.2. Micro-Morphology of Hole Wall with 45° Fiber Orientation

Figure 21 shows the hole wall micro-morphology under CD, L-UAD, and LTC-UAD at a fiber orientation of 45°. In Figure 21a, fiber fracture occurs above the machined surface, so overhanging fibers can be clearly observed. Serrated machined surfaces are visible in Figure 21b,c, and such serrated features are more prominent under L-UAD. The introduction of ultrasonic vibration increases the maximum cutting depth and alters the direction of cutting velocity, which shifts fiber fracture cross-sections beneath the machined surface. In addition, fibers are primarily removed via shear fracture, resulting in relatively flat fiber fracture cross-sections for all three machining conditions.

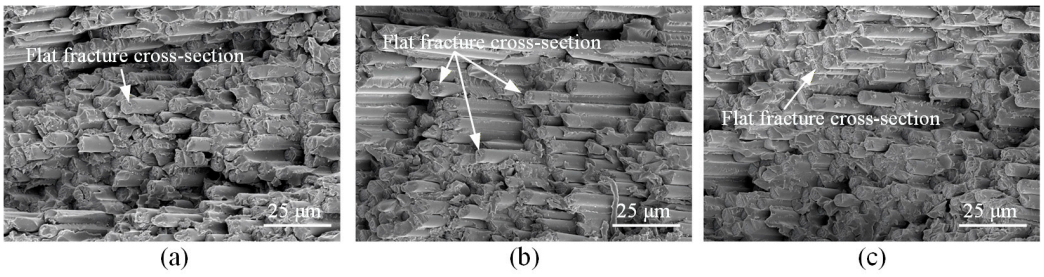

Figure 21. Micro-morphology of hole wall with 45° fiber orientation: (**a**) CD, (**b**) L-UAD, (**c**) LTC-UAD.

5.2.3. Micro-Morphology of Hole Wall with 90° Fiber Orientation

Figure 22 presents the hole wall micro-morphology under CD, L-UAD, and LTC-UAD with a fiber orientation of 90°. In Figure 22a, the bending fracture position of fibers lies deep below the machined surface, and the fiber fracture cross-sections are situated beneath the machined surface, thereby forming surface cavities. In Figure 22b, fibers fracture under the cutting action and the high-frequency impact of the cutting edge, and the actual fiber fracture depth becomes shallower, yielding improved machined surface quality. Nevertheless, residual fiber fragments can still be observed on the hole wall. In Figure 22c, the actual fiber fracture depth is further reduced. Moreover, the elliptical motion trajectory of the cutting edge facilitates the separation of chips and fiber fragments from the machined surface, so a higher-quality finished surface is obtained.

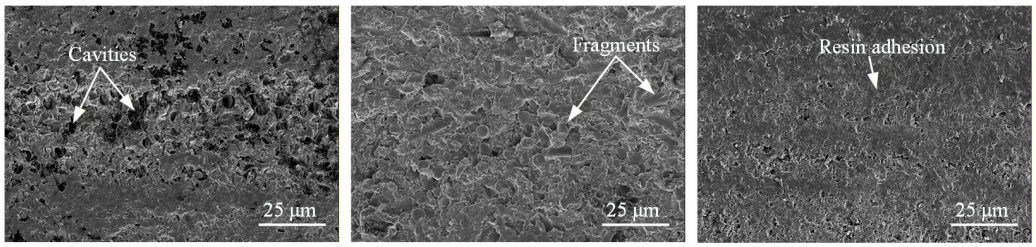

Figure 22. Micro-morphology of hole wall with 90° fiber orientation: (**a**) CD, (**b**) L-UAD, (**c**) LTC-UAD.

5.2.4. Micro-Morphology of Hole Wall with 135° Fiber Orientation

In CD, numerous bare fibers are exposed on the hole wall owing to insufficient resin coating induced by the harsh cutting behavior, as shown in Figure 23a. The introduction of ultrasonic vibration effectively improves this defective condition. As shown in Figure 23b, the resin coating area is significantly enlarged, which efficiently reduces the microscopic roughness of the hole wall. In Figure 23c, the unique elliptical cutting trajectory of longitudinal-torsional composite ultrasonic vibration achieves uniform resin adhesion. Only a few tiny cavities remain on the hole wall, presenting superior machined surface quality.

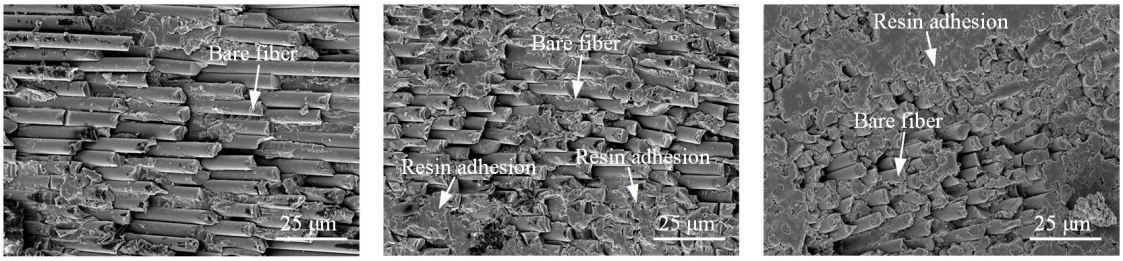

Figure 23. Micro-morphology of hole wall with 135° fiber orientation: (**a**) CD, (**b**) L-UAD, (**c**) LTC-UAD.

5.3. Thrust Forces

As shown in Figure 24, the thrust force under the two ultrasonic vibration-assisted drilling processes is significantly lower than that of CD. Compared with CD, the thrust force is reduced by 10.6% in L-UAD, while a reduction of 17.1% is achieved in LTC-UAD. In the drilling process, the primary cutting motion refers to the circumferential rotation of the main cutting edge, and the material removal at the hole bottom is realized by the tangential cutting of the main cutting edge. The axial motion of the drill bit only provides continuous feed to maintain stable cutting. For L-UAD, ultrasonic vibration is applied along the axial direction of the drill bit, which leads to a sinusoidal variation of instantaneous cutting

depth. When the main cutting edge moves toward an increased cutting depth, the flank face impacts the material at the hole bottom. When the cutting depth decreases, the rake face generates an upward lifting effect on the workpiece material, which reduces the average thrust force. In addition, according to the analysis in Section 2, longitudinal ultrasonic vibration enables the chisel edge to impact the hole-bottom material and improves the cutting condition near the chisel edge. Unlike L-UAD, LTC-UAD imposes both axial and tangential ultrasonic vibrations on the main cutting edge. The torsional vibration is superimposed on the primary cutting velocity, producing variable-speed cutting and variable-direction shearing behaviors. These characteristics facilitate the shear fracture of carbon fibers. Given that the shear strength of carbon fiber is much lower than its tensile strength, the longitudinal-torsional coupled vibration further reduces the thrust force.

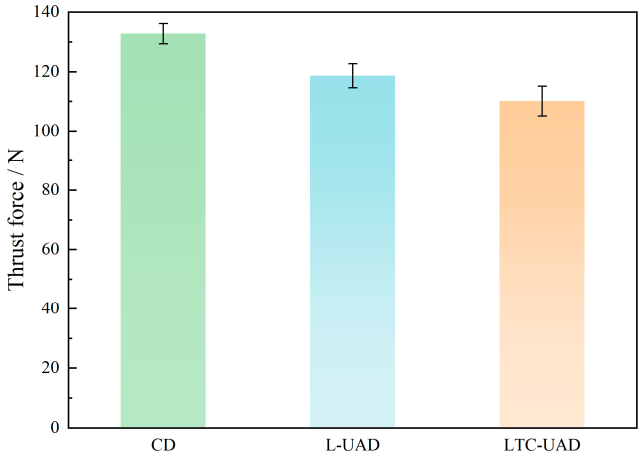

Figure 24. Thrust force under CD, L-UAD and LTC-UAD of CFRP.

6. Conclusions

This work reveals the superiority of LTC-UAD for CFRP drilling via kinematic analysis, finite element simulation and drilling experiments, taking CD and L-UAD as comparisons. Key conclusions are summarized below:

1. Compared with the spiral trajectory of CD and sinusoidal spiral of L-UAD, LTC-UAD produces an elliptical composite cutting path by coupling axial and torsional ultrasonic vibration. Coupled vibration periodically changes the cutting angle, greatly increasing and homogenizing the maximum working rake angle along the main cutting edge. The improvement is most significant near the chisel edge, narrowing the rake angle fluctuation range and optimizing cutting conditions.
2. Simulations at four fiber orientations (0°, 45°, 90°, 135°) show CD removes fibers mainly by deep subsurface bending fracture, causing uneven residual fibers and surface pits. 1D UVC introduces periodic cutting depth and high-frequency impact to form mixed shear-bending fracture, reducing fiber deformation and fracture depth but failing to avoid secondary fiber extrusion. The elliptical trajectory of 2D UVC aligns cutting velocity perpendicular to fibers, strengthens shear fracture, shortens subsurface damage and accelerates chip evacuation to eliminate secondary extrusion damage.
3. Micro-morphology of hole walls partially validates the above findings. CD leads to severe defects including fiber crushing, bare fibers and deep cavities. L-UAD relieves these defects partially but retains residual fiber fragments and serrated textures. LTC-UAD's elliptical trajectory enhances hole wall scraping and polishing, removes fiber debris, and forms uniform resin coverage, with only a few microcavities left and remarkably improved surface integrity.

4. Ultrasonic vibration can effectively suppress the thrust force during drilling of CFRP. Relative to CD, L-UAD reduces the thrust force by 10.6%, while LTC-UAD delivers a 17.1% reduction. The axial vibration in L-UAD introduces periodic fluctuation of instantaneous cutting depth and improves the cutting state of the chisel edge. The combined axial and torsional vibration of LTC-UAD facilitates shear fracture of carbon fibers, which accounts for its superior performance in thrust force reduction.

Author Contributions: Conceptualization, G.M. and M.Z.; methodology, G.Y. and G.M.; validation, G.Y., M.Z. and Y.C.; investigation, G.Y. and L.Z.; resources, G.Y.; data curation, Y.C.; writing—original draft preparation, G.Y. and M.Z.; writing—review and editing, G.Y. and Y.C.; visualization, Y.C. and L.Z.; supervision, G.M.; project administration, G.M. All authors have read and agreed to the published version of the manuscript.

Funding: This research received no external funding.

Data Availability Statement: Data are contained within the article.

Conflicts of Interest: The author Guolin Yang was employed by the company Longcheng Laboratory of Intelligent Manufacturing, Changzhou, China; The author Min Zhou and Yifan Cao was employed by the company Shanghai Aircraft Manufacturing Co., Ltd., Shanghai, China. The remaining authors declare that the research was conducted in the absence of any commercial or financial relationships that could be construed as a potential conflict of interest.

Abbreviations

The following abbreviations are used in this manuscript:

CFRP	Carbon fiber reinforced plastic
CD	Conventional drilling
L-UAD	Longitudinal ultrasonic vibration-assisted drilling
LTC-UAD	Longitudinal-torsional coupled ultrasonic vibration-assisted drilling
RVE	Representative volume element
1D UVC	One-dimensional ultrasonic vibration cutting
2D UVC	Two-dimensional ultrasonic vibration cutting

References

1. Geier, N.; Davim, J.P.; Szalay, T. Advanced cutting tools and technologies for drilling carbon fibre reinforced polymer (CFRP) composites: A review. *Compos. Part A Appl. Sci. Manuf.* **2019**, *125*, 105552. [CrossRef]
2. Liu, S.; Li, F.; Zuo, P.; Tian, H.; Xu, R.; Lv, L.; Huo, Y.; Yuan, Y.; Rao, H. Advancements in ultrafast laser processing of carbon fiber reinforced plastics: Mechanism, precision drilling, surface modification, and emerging applications. *Opt. Laser Technol.* **2025**, *192*, 113902. [CrossRef]
3. Luo, L.; Zhu, F.; Duan, L.; Zhao, F.; Zhang, Z. Surface quality and process optimization in rotary ultrasonic-assisted drilling of carbon-fiber-reinforced plastics. *Mech. Sci.* **2026**, *17*, 285–300. [CrossRef]
4. An, Q.L.; Dang, J.Q.; Li, J.L.; Wang, C.Y.; Chen, M. Investigation on the cutting responses of CFRP/Ti stacks: With special emphasis on the effects of drilling sequences. *Compos. Struct.* **2020**, *253*, 112794. [CrossRef]
5. Blanco, D.; Rubio, E.M.; Agustina, B.; Marín, M.M.; Camacho, A.M. Advanced procedures and scheduling for aircraft assembly processes: A systematic review approach. *Procedia CIRP* **2024**, *126*, 817–822. [CrossRef]
6. Zhang, S.; Wang, W.; Jiang, R.; Xiong, Y.; Huang, B.; Wang, J. Multi-objective optimization for the machining performance during ultrasonic vibration-assisted helical grinding hole of thin-walled CF/BMI composite laminates. *Thin Walled Struct.* **2023**, *192*, 111086. [CrossRef]
7. Poór, D.I.; Geier, N.; Pereszlai, C.; Xu, J. A critical review of the drilling of CFRP composites: Burr formation, characterisation and challenges. *Compos. Part B-Eng.* **2021**, *223*, 109155. [CrossRef]
8. Urresti-Espilla, I.; Telleria, M.; Llanos, I.; de Lacalle, L.N.L. CFRP drilling-induced defect investigation: Part quality characterization and process monitoring approach. *Int. J. Adv. Manuf. Technol.* **2025**, 1–14. [CrossRef]
9. Wang, T.; Liu, S.N.; Meng, Z.J.; Hu, K.Q.; Luo, B.; Zhang, K.F. Investigation on Hole Quality and Tool Wear of CFRP Drilling with Cryogenic-Minimal Quantity Lubrication. *Polym. Compos.* **2025**, *46*, 15666–15683. [CrossRef]

10. Atif, M.; Wang, X.; Xie, L.; Giasin, K.; Ma, Y.; Jiang, C.; Koklu, U.; Sinke, J. Multiscale modelling and experimental analysis of ultrasonic-assisted drilling of GLARE fibre metal laminates. *Compos. Part A Appl. Sci. Manuf.* **2024**, *177*, 107962.
11. Giasin, K.; Atif, M.; Ma, Y.; Jiang, C.; Koklu, U.; Sinke, J. Machining GLARE fibre metal laminates: A comparative study on drilling effect between conventional and ultrasonic-assisted drilling. *Int. J. Adv. Manuf. Technol.* **2022**, *123*, 3657–3672.
12. Li, Y.; Jiao, F.; Zhang, Z.; Wang, X.; Niu, Y. Mechanical drilling force model for longitudinal ultrasonic vibration-assisted drilling of unidirectional CFRP. *J. Mater. Process. Technol.* **2023**, *319*, 118091.
13. Zhang, X.; Cao, S.; Wu, C.; Huang, W.; Yang, M.; Liu, Y.; Tang, Y. Dynamic force modeling and delamination analysis of thin-walled CFRPs by ultrasonic vibration assisted drilling. *J. Manuf. Process.* **2025**, *150*, 24–37. [CrossRef]
14. Xu, M.R.; Cao, L.C.; Li, J.X.; Ali, S.; Kurniawan, R.; Li, C.P.; Yu, L.Q.; Chen, S.; Ko, T.J. Experimental, modeling, and numerical simulation of ultrasonic assisted drilling of CFRP/Ti stacks. *J. Mater. Process. Technol.* **2025**, *133*, 97–117. [CrossRef]
15. Tian, Y.J.; Cao, H.K.; Yin, S.; Yin, Z.H. Study on surface quality in longitudinal-torsional composite ultrasonic vibration assisted drilling of CFRP/Ti stacks. *Int. J. Adv. Manuf. Technol.* **2026**, *142*, 1285–1298.
16. Gao, G.; Xia, Z.; Yuan, Z.; Xiang, D.; Zhao, B. Influence of longitudinal-torsional ultrasonic-assisted vibration on micro-hole drilling Ti-6Al-4V. *Chin. J. Aeronaut.* **2021**, *34*, 247–260. [CrossRef]
17. Tian, Y.; Zou, P.; Wang, X.; Ling, Y. Study on chip shapes in longitudinal-torsional composite ultrasonic vibration–assisted drilling of Ti-6Al-4V. *Int. J. Adv. Manuf. Technol.* **2023**, *128*, 5561–5571. [CrossRef]
18. Geng, D.X.; Zhang, D.Y.; Li, Z.; Liu, D.P. Feasibility study of ultrasonic elliptical vibration-assisted reaming of carbon fiber reinforced plastics/titanium alloy stacks. *Ultrasonics* **2017**, *75*, 80–90. [CrossRef] [PubMed]
19. Liu, Y.; Li, Q.N.; Qi, Z.C.; Chen, W.L. Defect suppression mechanism and experimental study on longitudinal torsional coupled rotary ultrasonic assisted drilling of CFRPs. *J. Manuf. Process.* **2021**, *70*, 177–192. [CrossRef]
20. Liu, S.; Zheng, K.; Li, H.; Cao, Z.; Zhao, S. Multi-Objective Optimization of Process Parameters in Longitudinal-Torsional Ultrasonic Vibration Face Grinding CFRP. *Machines* **2023**, *11*, 935. [CrossRef]
21. Wang, C.H.; Li, P.N.; Li, S.J.; Qiu, X.Y.; Niu, Q.L.; Li, C.P.; Ko, T.J. Study on the mechanism and performance of longitudinal-torsional ultrasonic vibration assisted drilling CFRP/Ti stack. *J. Manuf. Process.* **2023**, *92*, 453–465. [CrossRef]
22. Ma, G.F.; Kang, R.K.; Yin, S.; Wang, Y.D.; Dong, Z.G. Effect of amplitude ratios on hole quality in longitudinal-torsional coupled ultrasonic-assisted drilling of CFRP composites. *Int. J. Adv. Manuf. Technol.* **2022**, *122*, 2911–2926. [CrossRef]
23. Wang, D.; Li, Z.; Tian, S.; Li, T. Study on dynamic drilling forces of CFRP/Ti stacks during longitudinal-torsional ultrasonic vibration drilling. *Int. J. Adv. Manuf. Technol.* **2023**, *126*, 2989–3004. [CrossRef]
24. Li, P.; Sun, J.; Li, J.; Zhang, R.; Chen, G. Study on drilling force and export defects of CFRP composites in RULTVD. *J. Manuf. Process.* **2025**, *134*, 880–890. [CrossRef]
25. Yan, X.; Zhang, K.; Cheng, H.; Luo, B.; Hou, G. Force coefficient prediction for drilling of UD-CFRP based on FEM simulation of orthogonal cutting. *Int. J. Adv. Manuf. Technol.* **2019**, *104*, 3695–3716. [CrossRef]
26. Xu, W.; Zhang, L.C.; Wu, Y. Elliptic vibration-assisted cutting of fibre-reinforced polymer composites: Understanding the material removal mechanisms. *Compos. Sci. Technol.* **2014**, *92*, 103–111. [CrossRef]
27. Zhang, P.; Wang, C.; Ying, Z.; Sugita, N. Improved cutting mechanism and surface generation of CFRP with ultrasonic vibration. *Precis. Eng.* **2026**, *99*, 440–452. [CrossRef]
28. Kaddour, A.S.; Hinton, M.J.; Smith, P.A.; Li, S. Mechanical properties and details of composite laminates for the test cases used in the third world-wide failure exercise. *J. Compos. Mater.* **2013**, *47*, 2427–2442. [CrossRef]
29. Vaughan, T.J.; McCarthy, C.T. Micromechanical modelling of the transverse damage behaviour in fibre reinforced composites. *Compos. Sci. Technol.* **2011**, *71*, 388–396. [CrossRef]

Disclaimer/Publisher's Note: The statements, opinions and data contained in all publications are solely those of the individual author(s) and contributor(s) and not of MDPI and/or the editor(s). MDPI and/or the editor(s) disclaim responsibility for any injury to people or property resulting from any ideas, methods, instructions or products referred to in the content.